Version of Record: https://www.sciencedirect.com/science/article/pii/S0304399121000772
Manuscript_a933baa4caa4c50fec99f698c20044ad

Gradient-based and wavelet-based compressed sensing approaches for highly undersampled tomographic datasets.

Martin Jacob[1], Loubna El Gueddari[2], Jyh-Miin Lin[1], Gabriele Navarro[1], Audrey Jannaud[1], Guido Mula[3], Pascale Bayle-Guillemaud[4], Philippe Ciuciu[2] and Zineb Saghi[1*]

[1] Univ. Grenoble Alpes, CEA, LETI, Grenoble F-38000, France.
[2] Univ. Paris Saclay, CEA-NeuroSpin, INRIA, Parietal, Gif-sur-Yvette, F-91191, France.
[3] Dipartimento di Fisica, Cittadella Universitaria di Monserrato, Università degli Studi di Cagliari, S.P. 8 km 0.700, 09042, Monserrato (Ca), Italy.
[4] Univ. Grenoble Alpes, CEA, IRIG, Grenoble F-38000, France.

E-mail address:

martin.jacob@cea.fr (Martin Jacob), loubna.elgueddari@gmail.com (Loubna El Gueddari), jyhmiinlin@gmail.com (Jyh-Miin Lin), Gabriele.navarro@cea.fr (Gabriele Navarro), audrey.jannaud3@cea.fr (Audrey Jannaud), guido.mula@dsf.unica.it (Guido Mula), pascale.bayle-guillemaud@cea.fr (Pascale Bayle-Guillemaud), Philippe.ciuciu@cea.fr (Philippe Ciuciu), zineb.saghi@cea.fr (Zineb Saghi)

***Corresponding author :**

Zineb Saghi
Commissariat à l'énergie atomique et aux énergies alternatives
MINATEC Campus
17 rue des martyrs
F-38054
Grenoble Cedex 9.
Tel: +33 (4) 38 78 48 70
Email: zineb.saghi@cea.fr

Abstract

Electron tomography is widely employed for the 3D morphological characterization at the nanoscale. In recent years, there has been a growing interest in analytical electron tomography (AET) as it is capable of providing 3D information about the elemental composition, chemical bonding and optical/electronic properties of nanomaterials. AET requires advanced reconstruction algorithms as the datasets often consist of a very limited number of projections. Total variation (TV)-based compressed sensing approaches were shown to provide high-quality reconstructions from undersampled datasets, but staircasing artefacts can appear when the assumption about piecewise constancy does not hold. In this paper, we compare higher-order TV and wavelet-based approaches for AET applications and provide an open-source Python toolbox, *Pyetomo*, containing 2D and 3D implementations of both methods. A highly sampled STEM-HAADF dataset of an Er-doped porous Si sample and a heavily undersampled STEM-EELS dataset of a Ge-rich GeSbTe (GST) thin film annealed at 450°C are used to evaluate the performance of the different approaches. We show that polynomial annihilation with order 3 ($HOTV_3$) and the Bior4.4 wavelet outperform the classical TV minimization and the related Haar wavelet.

Keywords:

Electron tomography, compressed sensing, total variation, wavelets, STEM-EELS/EDX tomography.

1. Introduction

Electron tomography (ET) based on high-angle annular dark-field scanning transmission electron microscopy (STEM-HAADF) mode is widely used in materials science for the 3D morphological analysis of objects at the nanoscale [1-3]. Recent advances in hardware have allowed the development of analytical ET (AET), which is the extension of ET to spectroscopic signals such as energy dispersive x-ray spectroscopy (EDX) and electron energy loss spectroscopy (EELS) [4-8]. AET provides significant insights into nanomaterials'

3D elemental composition, chemical bonding, and optical/electronic properties. However, due to the cross-sections for inelastic electron scattering and X-ray generation, it necessitates longer acquisition times and higher electron doses than STEM-HAADF tomography. Therefore, to minimize the total acquisition time and beam damage, AET datasets often consist of spectrum image datacubes acquired with a low signal-to-noise ratio and a relatively large tilt increment of 5° to 10°. Under these noisy and undersampled conditions, conventional reconstruction algorithms are not suitable as they yield poor image quality reconstructions with fanning artefacts. Various approaches have been proposed to overcome these intrinsic limitations: in [9], the convex hull of an object was estimated by geometric tomography from its binarised STEM-HAADF projections and used to mask the fanning artefacts present in the STEM-EDX reconstructions. Later, Zhong et al. introduced a bimodal HAADF-EDX tomography (HEBT) technique that combined STEM-HAADF and STEM-EDX data into one tomographic reconstruction process [10]. HEBT is suitable for samples where the following assumptions are fulfilled: (1) both STEM-HAADF and STEM-EDX datasets satisfy the projection requirement, and (2) the STEM-HAADF datasets are the weighted sum of the elemental maps for all elements present in the sample. The first implementation of HEBT [10] used the simultaneous iterative reconstruction technique (SIRT) algorithm, yielding STEM-HAADF and STEM-EDX reconstructions that were still affected by fanning artefacts. Recent algorithmic developments using the compressed sensing (CS) framework [11-12] have shown promising results for reconstructing volumes from heavily undersampled datasets [13-15] and are becoming increasingly popular for AET applications. These approaches exploit the object's sparsity in a chosen transform domain and employ the $l1$-norm minimization to recover a sparse solution under an $l2$-norm data consistency constraint. The choice of the sparsifying transform reflects the prior knowledge we have about the object to reconstruct. The $l1$-norm of the gradient is commonly called Total Variation (TV) minimization [16] and has been employed for the 3D chemical analysis of various nanomaterials using EELS [6,17], EDX [18] or both modalities [7]. TV promotes sparsity in the gradient domain and is very well suited for objects with piecewise constant regions and sharp edges. Since only the first derivative of the object is considered, staircasing artefacts are observed when the assumption about piecewise constancy does not hold. Moreover, recent studies have shown that TV's performance is highly dependent on the structural complexity of the object and the noise level [19-20].

The incorporation of higher-order derivatives has been proposed to overcome these drawbacks. Total Generalized Variation (TGV) [21-22] and polynomial annihilation edge detection methods [23], referred to as HOTV (High Order TV), promote piecewise smooth solutions while preserving sharp edges. These approaches have been applied to STEM-HAADF [24] and STEM-EDX [25] datasets with improved performances compared to TV. Joint HAADF and spectroscopic reconstructions using TV and TGV have also been proposed to improve the reconstructions' quality, but this strategy is restricted to objects with boundaries recovered in both modalities [25-26].

Wavelet-based CS methods are widely used in MRI [27-29] and have been applied in TEM mainly for denoising [30-31] and inpainting purposes [32-33]. They have recently gained interest in X-ray tomography [34] and ET [13, 35, 36], as they apply to a broader range of objects than gradient-based methods. However, only gradient-based methods have thus far been made accessible to the community via open-source packages (e.g. [24-25]).

In this work, we present an open-source toolbox, *Pyetomo*, where we implemented both gradient-based and wavelet-based methods for 2D slice-by-slice and 3D tomographic reconstructions. The current version of *Pyetomo* allows the testing of all the wavelet families built in the Pywavelet library, and makes use of cutting edge optimization algorithms initially developed for MRI and astrophysics applications [28, 37].

Using this toolbox, we compare the performance of gradient-based and wavelet-based approaches on a test object and assess the quality of the reconstructions of an undersampled AET dataset. Instead of generating a tilt series from a simulated test object, we use a highly sampled STEM-HAADF dataset of an Er-doped porous Si sample. This material has photoluminescence emission properties that can be tailored by controlling the sample's porosity (3D size, volume and distribution of the pores) and the Erbium distribution within the porous structure. STEM-HAADF tomography has contributed to a better understanding of these structures, as reported in [38-39]. In this work, reference reconstructions from 180 projections are generated and used to evaluate the performances of the different approaches as the number of projections decreases.

The different CS approaches are then applied to the 3D STEM-EELS analysis of a Ge-rich GeSbTe (GST) thin film annealed at 450°C. GST compounds have been widely utilized for phase-change memory (PCM) applications. They exhibit interesting properties, including a fast and reversible switch between an amorphous state and a crystalline state, a large

resistivity difference between these two states and a high crystallization temperature [40]. Ge-rich GST materials are of particular interest for applications at high temperatures as they were shown to yield higher thermal stability and better data retention than standard GST compounds such as $Ge_2Sb_2Te_5$ [41-42]. Recent studies have investigated the phase separation process in these alloys at different annealing temperatures [43-44]. Although advanced TEM techniques were employed, the interpretation of the results is hampered by the projection effect. Here, we employ STEM-EELS tomography to obtain information about the volume fraction of the two phases and their 3D distribution within the analyzed volume.

2. Methods

2.1 Compressed sensing methods applied to electron tomography

ET aims to reconstruct a 3D object from 2D projections acquired at different tilt angles with a TEM. When the projection requirement is fulfilled, each acquired pixel's intensity is approximately a line integral of a physical property of the object to be reconstructed. The set of projections correspond to the Radon transform of the object. The projection slice theorem states that the Fourier transform of a projection at an angle θ is a slice across the Fourier Transform of the original object at the same angle θ. This enables to formulate the reconstruction problem either in the image domain or in the Fourier domain. Analytical reconstruction approaches, such as filtered back-projection (FBP), aim to recover the object by inverting the Radon transform. These methods yield unsatisfactory reconstructions in the presence of noise and with a limited number of projections.

Iterative methods treat ET as an inverse problem, using the following discrete expression of the forward model:

$$Px = y \qquad (1)$$

Where x is the object to reconstruct, P the projection matrix and y the experimental projections. The most widely used iterative method is the simultaneous iterative reconstruction technique (SIRT) which solves the following least-squares problem:

$$\underset{x}{argmin}\left\{\frac{1}{2}\|Px - y\|_2^2\right\} \quad (2)$$

Reconstructions obtained with iterative methods are also degraded with increasing undersampling as the problem becomes severely ill-posed. A way to stabilize it is to incorporate prior knowledge about the solution x:

$$\underset{x}{argmin}\left\{\frac{1}{2}\|Px-y\|_2^2+\lambda R(x)\right\} \qquad (3)$$

This so-called variational formulation contains a data consistency term $\|Px-y\|_2^2$ and a regularisation term $R(x)$ which represents the prior information about x. The parameter λ controls the balance between the two terms. $R(x)=\|x\|_2^2$ corresponds to the minimal energy solution to the inverse problem. This regularisation is not sufficient for tomographic reconstruction with an undersampled dataset as it produces images with over-smoothed features. $R(x)=\|Lx\|_0$ promotes sparsity of x in the transform domain L (few non-zero elements in Lx). In the framework of CS, it was shown that under certain conditions (including sparsity of x in L and incoherence of L and P), the l_0 *quasi*-norm could be replaced by its convex envelope l_1 norm, leading to a convex optimization formulation:

$$\underset{x}{argmin}\left\{\frac{1}{2}\|Px-y\|_2^2+\lambda\|Lx\|_1\right\} \qquad (4)$$

In the *Pyetomo* toolbox, we implemented two types of transform domains:

- Gradient-based regularisations:

With $L=\nabla$, the regularisation term in Eq. (4) is the l_1 norm of the gradient of x, which is commonly called Total Variation (TV) minimization. TV promotes sparsity in the gradient domain and is very well suited for objects with piecewise constant regions and sharp edges.

Various TV expressions can be found in the literature, including isotropic, anisotropic, upwind [45] and directional forms [46]. In this paper, we choose the following anisotropic definition:

$$TV(x)=\int |\nabla x|_1 dudv \qquad (5)$$

Where $|\nabla x|_1 := |\nabla_u x|+|\nabla_v x|$, ∇_u and ∇_v being the horizontal and vertical partial derivative operators. For the isotropic form, as initially proposed by Rudin et al. [16], $|\nabla x|_1$ is replaced by $|\nabla x|_{2,1}=\sqrt{|\nabla_u x|^2+|\nabla_v x|^2}$.

Higher-order derivatives can be incorporated to extend the gradient-based approaches to piecewise-smooth objects. For example, the second-order total generalized variation (TGV) regularisation is defined as:

$$TGV(x) = \min_{w} \int_{\Omega} |\nabla x - w| du + \alpha \int_{\Omega} |\varepsilon(w)| du \qquad (6)$$

Where $\varepsilon(w)$ is the symmetric derivative, and α a weighting parameter that balances the effects of the first and the second derivatives [22].

Higher order TV (HOTV) is another approach that makes use of the polynomial annihilation transform [23]. In *Pyetomo*, we implemented HOTV of order *k*, as described in [24]. Note that HOTV of order 1 is equivalent to TV.

- Wavelet-based approaches:

The wavelet transform is based on a multiscale approximation of an object with dilation of a factor 2^j and shifting t of a scaling function ϕ, and the use of a similarly dilated and translated mother wavelet function ψ to retrieve the details between different approximation levels. The wavelet transform of a 1D signal, with a decomposition level l, can be written as:

$$x = \sum_{t=0}^{2^l-1} \langle x, \phi_{l,t} \rangle \phi_{l,t} + \sum_{j=l}^{n-1} \sum_{t=0}^{2^j-1} \langle x, \psi_{j,t} \rangle \psi_{j,t} \qquad (7)$$

with $\phi_{l,t}(u) = 2^{-l}\phi\left(2^{-l}u - t\right)$ and $\psi_{j,t}(u) = 2^{-j}\psi\left(2^{-j}u - t\right)$.

Or, under a compact form:

$$x = C_l + \sum_{j=l}^{n-1} W_j \qquad (8)$$

with C_l the approximation coefficients at scale l, and W_j the detail coefficients between scale j and j+1. This formulation can be extended to higher dimension signals such as images or volumes by separable products of the scaling function and the mother wavelet along the different dimensions. For instance, with a 2D signal and the same scaling and wavelet function, we have the 2D scaling function $\phi(u,v) = \phi(u)\phi(v)$ and the 2D wavelet functions $\psi^1(u,v) = \phi(u)\psi(v)$, $\psi^2(u,v) = \psi(u)\phi(v)$ and $\psi^3(u,v) = \psi(u)\psi(v)$.

In general, the choice of the most effective multiscale transform will depend on the prior knowledge we have about the object's features. However, some properties of the wavelet transform can help make a more appropriate one. For instance, a wavelet with a given

number of vanishing moments produces sparse transforms for signals that can locally be approximated by polynomials of degree inferior to this number. The symmetry of the chosen wavelet is also an interesting property that prevents distortion in the reconstructed signals. Standard orthogonal wavelets are not symmetric. To address this limitation, biorthogonal wavelets have been proposed: in this case, different functions are used for analysis (i.e. two scaling functions ϕ and ϕ' to generate a multiresolution analysis) and synthesis (two wavelet functions to reconstruct the signal or image). The biorthogonal transform remains invertible even though it is not necessarily orthogonal. Designing biorthogonal wavelets allows more degrees of freedom, particularly the possibility of constructing symmetric wavelet functions. We refer to the following textbooks for an extensive description of the different wavelets and their properties: [47-48].

In this paper, we use the Haar and the Bior4.4 biorthogonal wavelets with one and four vanishing moments at the analysis (4) and synthesis (4) steps, respectively. Figure 1 shows the Haar (a) and Bior4.4 (b) wavelet functions. Haar wavelet corresponds to Daubechies db1 wavelet. From its shape, the Haar wavelet can be seen as a multiscale gradient, providing an average image and the horizontal, vertical and diagonal gradients at each decomposition level. It is therefore adapted for piecewise constant objects, like TV. For features with a small anisotropy, biorthogonal wavelet transform is more appropriate. For highly anisotropic features, multiscale transforms based on anisotropic basis functions such as ridgelets, curvelets and shearlets, were shown to perform better than isotropic wavelets [49].

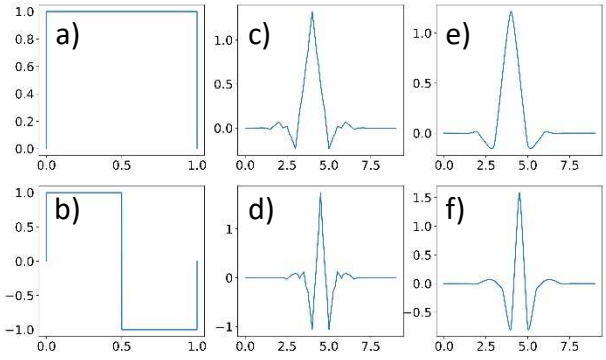

Figure 1 Haar scaling (a) and wavelet (b) functions; Bior4.4 analysis scaling (c) and wavelet (d) functions; Bior4.4 synthesis scaling (e) and wavelet (f) functions.

2.2 Pyetomo toolbox

The Python toolbox developed in this work is made available in this git repository: www.github.com/CEATomo/Pyetomo. It contains the 2D and 3D implementations of TV, HOTV, and wavelets using the PyWavelets library [50]. For the data consistency term, we used the Non-Uniform Fast Fourier Transform (NUFFT) operator and its adjoint, implemented in the PyNUFFT package [51]. Various algorithms have been proposed in the literature to solve the optimization problem in the CS reconstruction (Eq. (4)) [52]. In this work, we used the Condat-Vu primal-dual splitting method, included in the ModOpt package [37]. A non-negativity constraint was also added to the cost function. Figure 2 summarises the different features of the toolbox. We point out in italic the options that were not tested in this work but are included in the toolbox or can easily be imported: the proximal gradient methods are included in ModOpt; the Radon-based projection operator can be imported from Astra toolbox [53]; Sparse2D package can be imported from *https://github.com/CosmoStat/Sparse2D* for more advanced transforms [28].

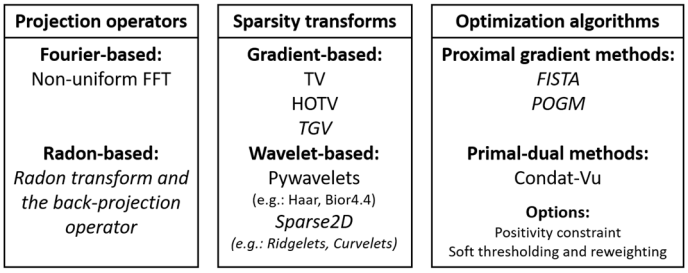

Figure 2 Projection operators, sparsity transforms, and optimization algorithms included in the toolbox *Pyetomo.* In italic are the features that are included but were not tested (FISTA, POGM), and those that can be easily incorporated in the future (TGV, the Radon operator and advanced wavelets from Sparse2D).

2.3 Experimental data acquisition and processing

2.3.1. STEM-HAADF tomography of Erbium-doped porous silicon

As reported in [38], a needle-shaped sample was prepared by focused ion beam (FIB) and mounted onto an on-axis tomography holder (Fischione model 2050). A full 180° tilt range tomographic dataset was acquired in a double-corrected Titan 80-300 kV STEM (Thermo Fisher Scientist) operated at 80kV, with a tilt increment of 1°, a frame size of 1024*1024 pixels and a pixel size of 0.41 nm. Figure 3(a) is the STEM-HAADF projection of the sample at 0° tilt angle. The tilt series alignment was performed following the procedure described in [39]. SIRT yielded a high-quality reconstruction with fine details about the pores and the Erbium clusters (Figure 3(b-e)). In this paper, we compared the CS reconstructions of a

selected slice (indicated in green in Figure 3(a)) using the 2D implementation of TV, HOTV, Haar and Bior4.4 sparse representations. For each of these methods, the 1° reconstruction was used as a reference image.

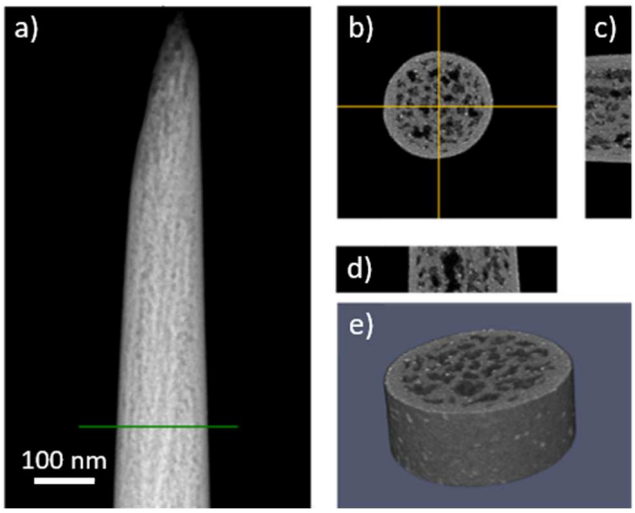

Figure 3 (a) 0° STEM-HAADF projection of the Er-doped Si sample. (b-d) selected xy, xz and yz orthoslices through the reconstructed subvolume. (e) Voxel rendering of the reconstructed subvolume.

2.3.2. STEM-EELS tomography of Ge-rich GST material annealed at 450°C

A needle-shaped sample of a Ge-rich GST thin film annealed at 450°C was prepared by FIB and transferred onto an on-axis tomography holder. STEM-EELS acquisition was performed at 200kV in a probe-corrected Titan 80-200 kV STEM (Thermo Fisher Scientist) equipped with a Quantum Gatan imaging filter. 18 STEM-EELS datacubes were acquired over a tilt range of 180°, with a pixel size of 2nm, a frame size of 100x75 pixels, and a dwell time of 0.1 sec/pixel for the energy range of 250-2398 eV. The overlapping of Sb $M_{4,5}$-edge (528 eV), O K-edge (532 eV) and Te $M_{4,5}$-edge (572eV), and the presence of Ge in both phases make the use of classical elemental analysis difficult (see Figure S2). We instead used vertex component analysis (VCA) to identify the different chemical components present in the hyperspectral dataset, including the SiN capping, the GST phase, the Ge phase, and the SiO_2 substrate. The extraction of the corresponding abundance maps was performed using the SUNSAL solver [54]. Figure 4(a) shows the 0° STEM-HAADF image and the region selected for the STEM-EELS experiment (inset in white). Figure 4(b) shows the spectral components of Ge (blue) and GST (red), and Figure 4(c) the corresponding abundance maps at -90°, 0° and +70°. The tilt series (which fulfil the projection requirement, as illustrated in Figure S3) were aligned and used as input for the CS reconstructions based on TV, HOTV,

Haar and Bior4.4 sparse representations. A video showing the aligned stacks can be found in the supplementary information (SI_movie_1).

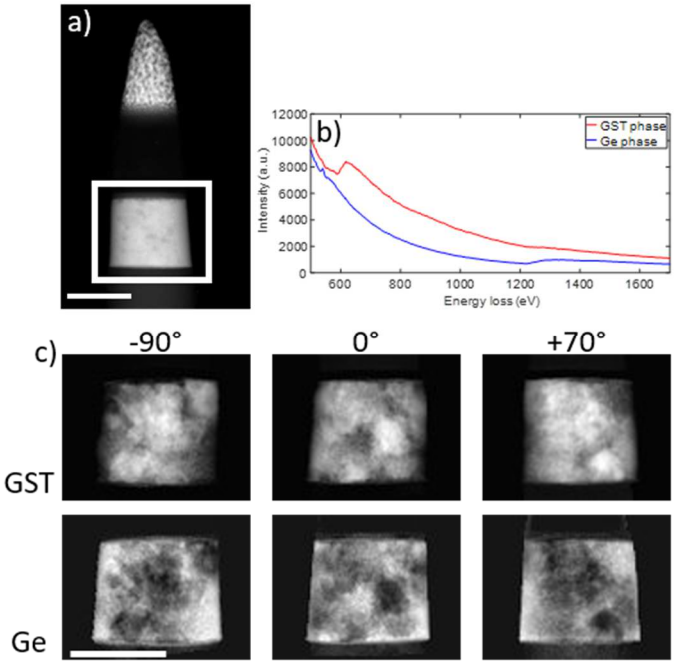

Figure 4 (a) 0° STEM-HAADF projection of the Ge-rich GST sample and the region (white inset) selected for the STEM-EELS experiment. (b) Spectral components corresponding to the Ge (blue) and GST (red) phases, as extracted by VCA. (c) GST (top) and Ge (bottom) abundance maps at -90°, 0° and +70°. Scale bar: 100 nm.

3. Results

3.1 Effect of undersampling

A selected slice through the Er-doped Si needle was reconstructed with the full STEM-HAADF dataset (180 projections), using the 2D implementation of TV, Haar wavelet,

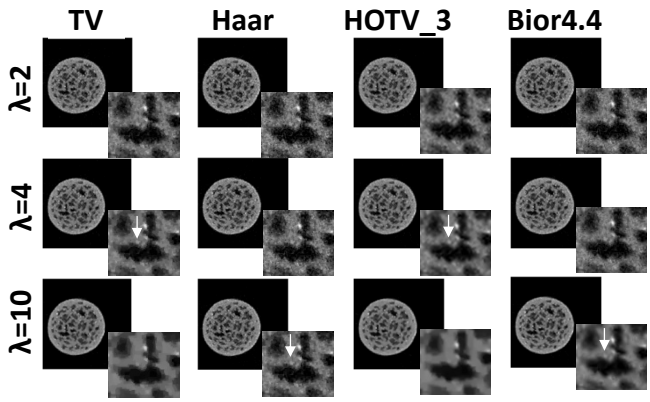

$HOTV_3$ (HOTV with order 3) and Bior4.4 sparse representations. The maximum number of iterations was set to 300, and the non-negativity constraint was added to the cost function. Different values of the regularisation parameter λ were tested. As shown in Figure 5, a small λ yielded reconstructions influenced mainly by the data fidelity term. By increasing λ, more weight was given to the regularization term, inducing artefacts specific to each sparse representation. Based on the visual quality assessment of the reconstructions, an optimal value of 4 for TV and $HOTV_3$ and 10 for Haar and Bior4.4 was selected.

Figure 5 Reconstructions of a selected slice in the Er-doped Si sample, using the 2D implementation of TV, Haar, $HOTV_3$, and Bior4.4 sparsity transforms. The optimal regularisation parameter λ was 4 for TV and $HOTV_3$, and 10 for Haar and Bior4.4, based on visual assessment (visibility of the small cluster indicated with the white arrow).

Reconstructions with datasets consisting of 90 (2° increment), 45 (4° increment), 36 (5° increment) and 18 (10° increment) projections were then performed and compared to the reconstructions with 180 projections. Figure 6(a) shows a selected region from the reconstructions. The normalized root mean square error (nRMSE) and structural similarity index (SSIM), as implemented in the module *metrics* from the scikit-image library, were used to assess the images' quality and evaluate the performance of the CS methods as a function of the angular increment (Figure 6(b,c)). Based on these metrics, we see that Bior4.4 yields improved results compared to TV and Haar regularisations, which exhibit the same behaviour and produce strongly degraded images as the angular increment increases. $HOTV_3$ lies between Bior4.4 and TV/Haar, with a relatively high nRMSE at 10° increment. Note that for each sparse representation, the corresponding fully sampled reconstruction was used as a reference image. As shown in Figure S1, selecting the same reference image for all CS

methods (the Bior4.4 reconstruction) yielded SSIM and nRMSE curves with the same trends as Figure 6 (b,c). These results are coherent with the visual assessment of the reconstructions: we notice that TV and Haar, which can be regarded as a multiscale version of TV, yield similar results and suffer from block artefacts when the dataset is heavily undersampled. This outcome is expected as both regularisations favour piecewise constancy. Bior4.4 eliminates these effects but induces smoothness as the tilt increment increases. $HOTV_3$ reconstructions exhibit noise-like spurious oscillations with a loss of contrast as the tilt increment increases but are visually more resolved than TV and Haar reconstructions, as reflected by the SSIM metric.

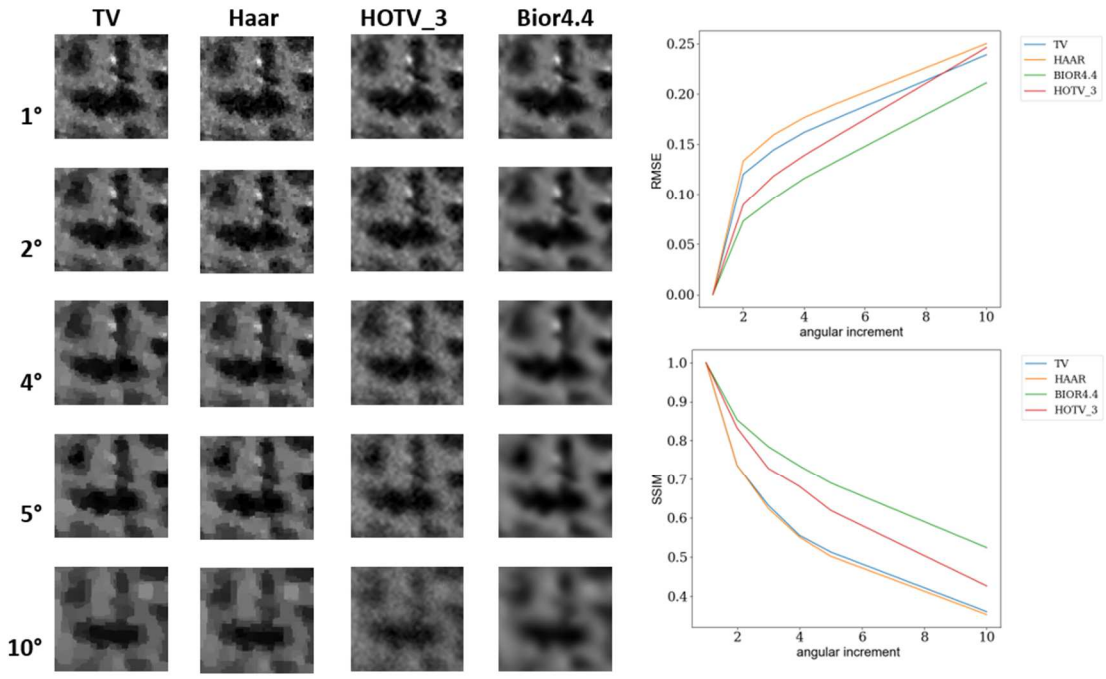

Figure 6 (a) TV, Haar, HOTV_3 and Bior4.4 reconstructions with 1°, 2°, 4°, 5° and 10° increments. (b) RMSE and (c) SSIM scores showing the evolution of the image quality as a function of the angular increment (in degrees).

The 2D porosity was also calculated for each reconstruction after automatic thresholding by Otsu's method. The absolute percentage error on the measurements, compared to the reference images' porosity (reconstructions using 1° increment), is plotted in Figure 7 as a function of tilt increment. We observe that below 3° increment, the absolute percentage error is less than 2% for all methods, with a slight advantage for $HOTV_3$. However, for large tilt

increments, Bior4.4 outperforms the other approaches as it shows the smallest deviations. $HOTV_3$ provides the worst quantitative measures, and we attribute this to the low SNR and contrast in the reconstructions, making the automated segmentation step more challenging.

Visually, we notice, regardless of the approach used for the reconstruction, that the Er clusters are unresolved for increments greater than 2°. These results suggest that the reconstruction algorithm and the experimental conditions have to be carefully adjusted according to the sample complexity and the information sought-after in the reconstructions. Since the Er clusters' size is close to the resolution limit of classical HAADF-STEM tomography, a large number of projections is necessary to study their distribution within the porous Si structure.

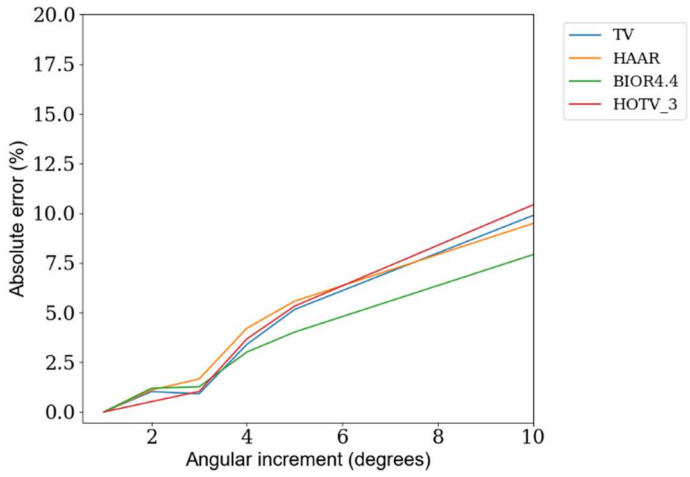

Figure 7 Absolute percentage error between the porosity estimated from the reconstructed images and the reference image (reconstruction from 180 projections).

3.2 CS methods applied to STEM-EELS datasets

The GST tilt series was used for the choice of the regularization parameter λ. Figure 8 shows the reconstructions of a selected xy slice using the 2D implementations with 300 iterations and the non-negativity constraint. We see that as λ increases, both TV and Haar yield flat, blocky GST regions and over-regularised edges. $HOTV_3$ and Bior4.4, on the other hand, preserve the surface roughness of the GST grains and recover fine details. $HOTV_3$ reconstruction shows fewer oscillations than in the STEM-HAADF reconstruction of the Er-doped Si sample. We can attribute this to the difference in dimensions of the STEM-HAADF (1024x1024 pixels) and STEM-EELS chemical phase (100x75 pixels) projections. The

correlation between the size of the images and the unwanted oscillations is discussed in more details in [55].

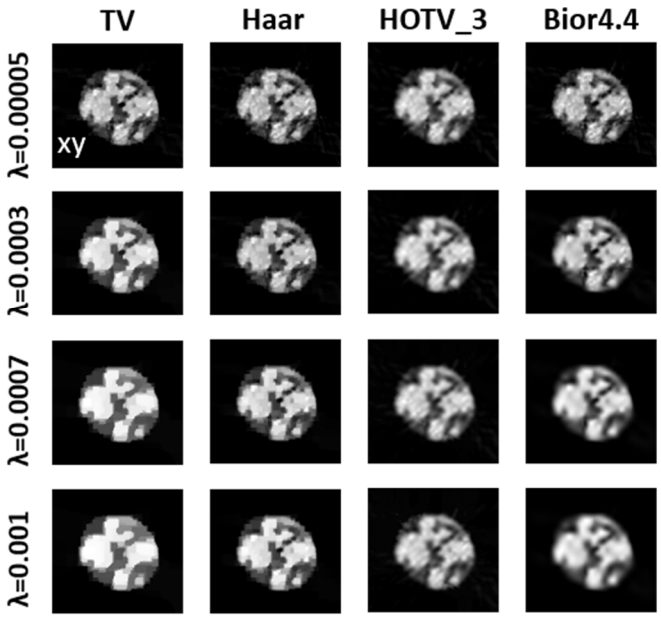

Figure 8 Reconstructions of a selected xy slice through the GST volume, using the 2D implementation of TV, Haar, $HOTV_3$, and Bior4.4 sparsity transforms, and different values for the regularisation parameter λ.

The 3D reconstructions of the Ge and GST volumes were performed using the 3D implementations of the four methods, with 300 iterations, the non-negativity constraint, and a λ value of 0.0003 for TV and HOTV, and 0.0007 for Haar and Bior4.4. Figure 9 shows the 3D rendering of the GST (in red) and Ge (in blue) volumes, and a video showing the slices through the TV and Bior4.4. reconstructions can be found in the supplementary information (SI_movie_2). As expected, the 3D implementations yield better reconstructions for HOTV and Bior4.4. than Haar and TV (see, for example, the region pointed out with the white arrow in the inset of the xz slices). The outer layer observed in all Ge reconstructions is attributed to a redeposition during the FIB sample preparation.

For a quantitative comparison of the reconstructions, we estimated the GST phase's volume fraction after automatic thresholding by Otsu's method. We found 0.491 for TV, 0.494 for Haar, 0.533 for $HOTV_3$ and 0.527 for Bior4.4. These values confirm the capability of TV and Haar on the one hand and $HOTV_3$ and Bior4.4 on the other in achieving similar results. Since $HOTV_3$ and Bio4.4 reconstructions are visually superior to Haar and TV, we can deduce that the true volume fraction is close to 0.53.

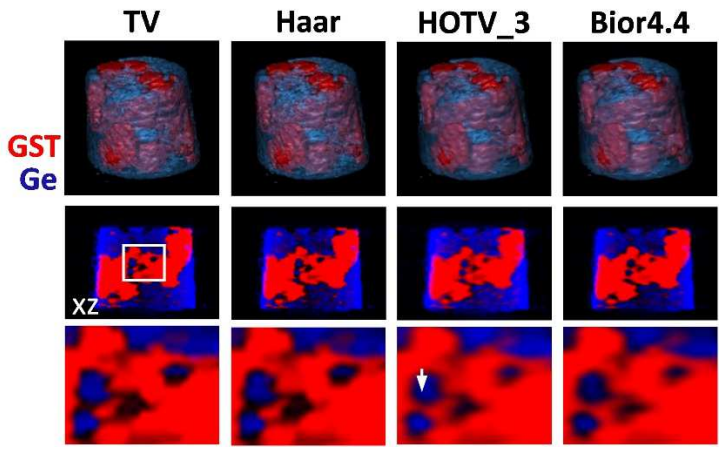

Figure 9 Reconstruction of GST and Ge phases using the 3D implementation of TV, Haar, HOTV$_3$ and Bior4.4. From top to bottom rows: volume rendering of the reconstructions; xz orthoslice through the reconstructions; zoomed images from the inset in the xz orthoslices.

In Figure 10, the 2D area fraction of the GST phase is plotted as a function of the sample depth. We observe a constant fraction at the top 5nm and the low part of the film (~ 0.44 for TV/Haar, and ~0.48 for HOTV_3/Bior4.4), and a higher fraction in the sub-volume between 10 and 45nm from the top, with a peak at 30nm reaching ~0.62 for TV/Haar and ~0.66 for HOTV_3/Bior4.4. This phase distribution along the sample depth is also apparent in the xz slices through the 3D reconstructions in Figure 9.

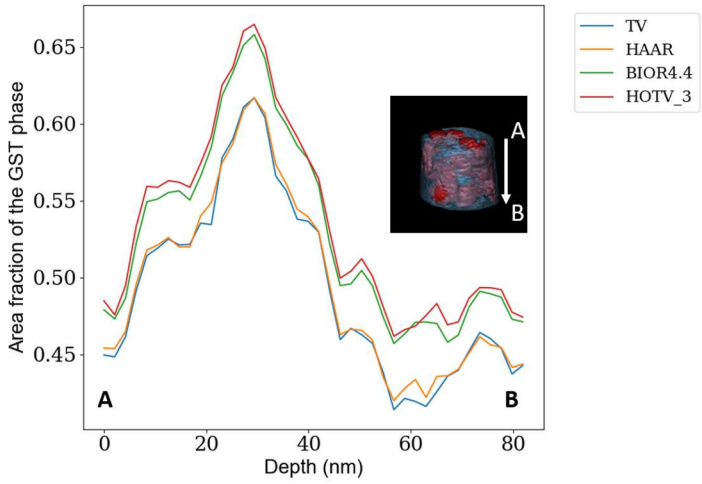

Figure 10 2D area fraction of the GST phase as a function of sample depth.

The shape of the GST grains and their inclusion in the Ge volume seem to support the hypothesis of nucleation and growth of the GST phase before the Ge phase's growth, once the demixing has taken place. We also note that both Ge and GST volumes contain pores,

which are visible in the STEM-HAADF projection, Figure 4(a). A similar study conducted on thin films annealed at 380°C and 400°C yielded the following conclusions: 1) the size of the pores increases with the annealing temperature; 2) the chemical segregation only happens at the top 60 nm of the thin film at 400°C, while no phase separation is observed at 380°C.

4. Discussion

In this work, we implemented gradient-based and wavelet-based reconstruction methods in the *Pyetomo* toolbox and applied them on STEM-HAADF and STEM-EELS datasets. TV and Haar yield very similar results and are mostly adapted for simple piecewise constant structures. TV and Haar are not suitable for more complex geometries and with heavily undersampled datasets. $HOTV_3$ approach outperforms these two methods as it eliminates the block artefacts but suffers from unwanted, noise-like oscillations, which makes the segmentation a challenging task. Our results confirm previous findings that the oscillations are related to the dimension of the reconstructed volume. Bior4.4 yields the best results for STEM-HAADF and STEM-EELS datasets and is in excellent agreement with $HOTV_3$ for the 3D quantification of the STEM-EELS reconstructions. We note that the reconstructions become over-smoothed as the tilt increment increases and that border artefacts can appear around the edges (see the Bior4.4 reconstruction with λ=10, in Figure 5). These limitations have been overcome in MRI and astrophysics by exploring anisotropic multiscale approaches such as ridglets, curvelets and shearlets [56]. These methods have not yet been explored in the field of electron tomography, but promising results were reported for the edge detection of vesicle membranes in a TEM image by curvelets [57] and inpainting of a high-resolution STEM-HAADF image of a complex oxide ceramic using shearlet transforms [33].

When the STEM-HAADF and the elemental or chemical phase maps share common features, a joint multi-channel approach can produce reconstructions from all signals simultaneously and with improved quality. While these approaches were reported using TV or TGV regularisations, we believe that wavelet-based regularisations can easily be incorporated into the existing codes, with the potential for further improvements of the reconstructions. Combining at least two sparsity transforms has also led to promising results (see for example [58-59]), and we intend to investigate this strategy for AET applications.

STEM-EELS tomography of the Ge-rich GST sample provided important 3D information about the chemical phase segregation process, which was hitherto exclusively studied in 2D.

The needle-shaped geometry allowed a full tilt range acquisition with no missing wedge artefacts but with a restricted field of view compared to classical FIB lamellae utilized for the 2D characterizations. CS methods do not allow for the correction of artefacts when the missing wedge is larger than 30°, as reported in [19, 35,60]. Strategies for sinogram inpainting have recently shown promising results (see for example [61-62]), but further work is required to investigate their effectiveness on complex objects.

Finally, for all CS methods, and in the absence of ground truth, the choice of the regularisation parameter λ is a difficult task with a significant impact on the reconstructions' quality. While it is common to adjust λ manually based on the visual evaluation of the reconstruction quality, a more in-depth assessment of the acquisition conditions and the nature of the noise can help automate this step [63].

5. Conclusion

In this work, we have presented the *Pyetomo* toolbox and used it to investigate the performance of gradient-based and wavelet-based CS techniques for the reconstruction of heavily undersampled datasets, with a particular interest for AET applications. As an example, STEM-EELS tomography was performed on a Ge-rich GST material to understand better the phase separation process occurring at high annealing temperatures. We showed that polynomial annihilation with order 3 ($HOTV_3$) and the Bior4.4 wavelet provide higher quality reconstructions than the classical TV minimization and the related Haar wavelet, making the segmentation and the quantification steps more reliable. Using an Er-doped Si structure as a test object, we also confirmed, as reported in [19], that the minimum number of projections required for a high-quality reconstruction strongly depends on the complexity of the object, regardless of the reconstruction algorithm.

In the future, we plan to (1) include denoising and inpainting routines based on the proposed methods, (2) accelerate the reconstructions with GPU implementations, and (3) explore the advanced transforms implemented in *Sparse2D* library.

We believe that *Pyetomo* toolbox will be of great interest not only for AET applications in the field of materials science, but also for the cryo-ET and X-ray tomography communities.

Acknowledgements:

This work was carried out at the Nanocharacterization Platform (PFNC) of Minatec, supported by the 'Recherche technologique de Base' program of the French Ministry of Research. We thank Tony Printemps for the acquisition of the porous Si dataset. We acknowledge the financial support of the Cross-Disciplinary Program on Numerical Simulation of CEA, the French Alternative Energies and Atomic Energy Commission.

References

[1] Z. Saghi and P. A. Midgley, 'Electron Tomography in the (S)TEM: From Nanoscale Morphological Analysis to 3D Atomic Imaging', *Annu. Rev. Mater. Res.* 2012, 42(1): 59–79.

[2] A. B. Hungría, J. J. Calvino and J. C. Hernández-Garrido, 'HAADF-STEM Electron Tomography in Catalysis Research', *Top. Catal.* 2019, 62(12): 808–821.

[3] R. K. Leary and P. A. Midgley, 'Electron Tomography in Materials Science', in *Springer Handbook of Microscopy*, P. W. Hawkes and J. C. H. Spence, Eds. Cham: Springer International Publishing, 2019.

[4] P. Burdet, Z. Saghi, A. N. Filippin, A. Borrás and P. A. Midgley, 'A novel 3D absorption correction method for quantitative EDX-STEM tomography', *Ultramicroscopy* 2016, 160: 118–129.

[5] R. K. Leary and P. A. Midgley, 'Analytical electron tomography', *MRS Bull.* 2016, 41(7): 531–536.

[6] S. M. Collins, E. Ringe, M. Duchamp, Z. Saghi, R. E. Dunin-Borkowski and P. A. Midgley, 'Eigenmode Tomography of Surface Charge Oscillations of Plasmonic Nanoparticles by Electron Energy Loss Spectroscopy', *ACS Photonics* 2015, 2(11): 1628–1635.

[7] G. Haberfehlner, A. Orthacker, M. Albu, J. Li and G. Kothleitner, 'Nanoscale voxel spectroscopy by simultaneous EELS and EDS tomography', *Nanoscale* 2014, 6(23): 14563–14569.

[8] S. M. Collins and P. A. Midgley, 'Progress and opportunities in EELS and EDS tomography', *Ultramicroscopy* 2017, 180: 133–141.

[9] Z. Saghi, X. Xu, Y. Peng, B. Inkson and G. Möbus, 'Three-dimensional chemical analysis of tungsten probes by energy dispersive x-ray nanotomography', *Appl. Phys. Lett.* 2007, 91: 251906.

[10] Z. Zhong, B. Goris, R. Schoenmakers, S. Bals and K. J. Batenburg, 'A bimodal tomographic reconstruction technique combining EDS-STEM and HAADF-STEM', *Ultramicroscopy* 2017, 174: 35–45.

[11] E. J. Candes, J. Romberg and T. Tao, 'Robust uncertainty principles: exact signal reconstruction from highly incomplete frequency information', *IEEE Trans. Inf. Theory* 2006, 52(2): 489–509.

[12] D. L. Donoho, 'Compressed sensing', *IEEE Trans. Inf. Theory* 2006, 52(4): 1289–1306.

[13] R. Leary, Z. Saghi, P. A. Midgley and D. J. Holland, 'Compressed sensing electron tomography', *Ultramicroscopy* 2013, 131: 70–91.

[14] B. Goris, W. Van den Broek, K. J. Batenburg, H. Heidari Mezerji and S. Bals, 'Electron tomography based on a total variation minimization reconstruction technique', *Ultramicroscopy* 2012, 113: 120–130.

[15] Z. Saghi *et al.*, 'Three-Dimensional Morphology of Iron Oxide Nanoparticles with Reactive Concave Surfaces. A Compressed Sensing-Electron Tomography (CS-ET) Approach', *Nano Lett.* 2011, 11(11): 4666–4673.
[16] L. I. Rudin, S. Osher, and E. Fatemi, 'Nonlinear total variation based noise removal algorithms', *Phys. Nonlinear Phenom.* 1992, 60(1): 259–268.
[17] P. Torruella *et al.*, '3D Visualization of the Iron Oxidation State in FeO/Fe3O4 Core–Shell Nanocubes from Electron Energy Loss Tomography', *Nano Lett.* 2016, 16(8): 5068–5073.
[18] J. F. Einsle *et al.*, 'Nanomagnetic properties of the meteorite cloudy zone', *Proc. Natl. Acad. Sci.* 2018, 115(49): E11436–E11445.
[19] Y. Jiang, E. Padgett, R. Hovden, and D. A. Muller, 'Sampling limits for electron tomography with sparsity-exploiting reconstructions', *Ultramicroscopy*, vol. 186, pp. 94–103, Mar. 2018, doi: 10.1016/j.ultramic.2017.12.010.
[20] J. Jorgensen, W. Lionheart, S. Mcdonald, and P. Withers, 'SparseBeads Data: Benchmarking sparsity-regularized computed tomography', *Meas. Sci. Technol.* 2017, 28: 124005.
[21] M. Benning, C. Brune, M. Burger and J. Müller, 'Higher-Order TV Methods—Enhancement via Bregman Iteration', *J. Sci. Comput.* 2013, 54(2): 269–310.
[22] F. Knoll, K. Bredies, T. Pock and R. Stollberger, 'Second Order Total Generalized Variation (TGV) for MRI', *Magn. Reson. Med.* 2011, 65(2): 480–491.
[23] R. Archibald, A. Gelb and R. Platte, 'Image Reconstruction from Undersampled Fourier Data Using the Polynomial Annihilation Transform', *J. Sci. Comput.* 2016, 67: 432-452.
[24] T. Sanders, A. Gelb, R. B. Platte, I. Arslan, and K. Landskron, 'Recovering fine details from under-resolved electron tomography data using higher order total variation ℓ1 regularization', *Ultramicroscopy* 2017, 174: 97–105.
[25] R. Huber, G. Haberfehlner, M. Holler, G. Kothleitner and K. Bredies, 'Total generalized variation regularization for multi-modal electron tomography', *Nanoscale* 2019, 11(12): 5617–5632.
[26] Z. Zhong, W. J. Palenstijn, J. Adler and K. J. Batenburg, 'EDS tomographic reconstruction regularized by total nuclear variation joined with HAADF-STEM tomography', *Ultramicroscopy* 2018, 191: 34–43.
[27] M. Lustig, D. Donoho and J. M. Pauly, 'Sparse MRI: The application of compressed sensing for rapid MR imaging', *Magn. Reson. Med.* 2007, 58(6): 1182–1195.
[28] H. Cherkaoui *et al.*, 'Analysis vs Synthesis-based Regularization for Combined Compressed Sensing and Parallel MRI Reconstruction at 7 Tesla', *26th European Signal Processing Conference (EUSIPCO)* 2018, 36–40.
[29] J. C. Ye, 'Compressed sensing MRI: a review from signal processing perspective', *BMC Biomed. Eng.* 2019, 1(1): 8.
[30] X. Huang, S. Li, and S. Gao, 'Exploring an optimal wavelet-based filter for cryo-ET imaging', *Sci. Rep.* 2018, 8: 2582.
[31] C. Sorzano, E. Ortiz, M. López, and J. Rodrigo, 'Improved Bayesian image denoising based on wavelets with applications to electron microscopy', *Pattern Recognit.* 2006, 39: 1205–1213.
[32] X. Li, O. Dyck, S. Kalinin and S. Jesse, 'Compressed Sensing of Scanning Transmission Electron Microscopy (STEM) With Nonrectangular Scans', *Microsc. Microanal.* 2018, 24: 623–633.
[33] D. Mucke-Herzberg *et al.*, 'Practical Implementation of Compressive Sensing for High Resolution STEM', *Microsc. Microanal.* 2016, 22(S3): 558–559.

[34] J. F. P. J. Abascal *et al.*, 'Sparse reconstruction methods in x-ray CT', *Proc. SPIE* 2017, 10391: 1039112.
[35] M. D. Guay, W. Czaja, M. A. Aronova, and R. D. Leapman, 'Compressed Sensing Electron Tomography for Determining Biological Structure', *Sci. Rep.* 2016, 6: 27614.
[36] O. Nicoletti, F. de la Peña, R. K. Leary, D. J. Holland, C. Ducati and P. A. Midgley, 'Three-dimensional imaging of localized surface plasmon resonances of metal nanoparticles', *Nature* 2013, 502: 7469.
[37] S. Farrens *et al.*, 'PySAP: Python Sparse Data Analysis Package for multidisciplinary image processing', *Astron. Comput.* 2020, 32: 100402.
[38] G. Mula *et al.*, 'Doping porous silicon with erbium: pores filling as a method to limit the Er-clustering effects and increasing its light emission', *Sci. Rep.* 2017, 7: 5957.
[39] T. Printemps *et al.*, 'Self-adapting denoising, alignment and reconstruction in electron tomography in materials science', *Ultramicroscopy* 2016, 160: 23–34.
[40] M. Wuttig and N. Yamada, 'Phase-change materials for rewriteable data storage', *Nat. Mater.* 2007, 6: 824–832.
[41] G. Navarro *et al.*, 'Phase-Change Memory: Performance, Roles and Challenges', *IEEE International Memory Workshop* 2018, 1–4.
[42] V. Sousa *et al.*, 'Operation fundamentals in 12Mb Phase Change Memory based on innovative Ge-rich GST materials featuring high reliability performance', *Symposium on VLSI Technology* 2015, T98–T99.
[43] M. Agati, F. Renaud, D. Benoit and A. Claverie, 'In-situ transmission electron microscopy studies of the crystallization of N-doped Ge-rich GeSbTe materials', *MRS Commun.* 2018, 8(3): 1145–1152.
[44] M. Agati, M. Vallet, S. Joulié, D. Benoit and A. Claverie, 'Chemical phase segregation during the crystallization of Ge-rich GeSbTe alloys', *J. Mater. Chem. C* 2019, 7(28): 8720–8729.
[45] L. Condat, 'Discrete Total Variation: New Definition and Minimization', *SIAM J. Imaging Sci.* 2017, 10: 1258–1290.
[46] O. Merveille, B. Naegel, H. Talbot and N. Passat, 'nD Variational Restoration of Curvilinear Structures With Prior-Based Directional Regularization', *IEEE Trans. Image Process.* 2019, 28(8): 3848–3859.
[47] S. Mallat, *A Wavelet Tour of Signal Processing, Third Edition: The Sparse Way*, 3rd ed. Orlando, FL, USA: Academic Press, Inc., 2008.
[48] J.L. Starck, F. Murtagh and J. Fadili, *Sparse Image and Signal Processing: Wavelets and Related Geometric Multiscale Analysis*, 2nd ed. Cambridge University Press, 2015.
[49] J.L. Starck, D. L. Donoho and E. J. Candès, 'Astronomical image representation by the curvelet transform', *Astron. Astrophys.* 2003, 398: 785-800.
[50] G. Lee, R. Gommers, F. Waselewski, K. Wohlfahrt and A. O'Leary, 'PyWavelets: A Python package for wavelet analysis', *J. Open Source Softw.* 2019, 4(36): 1237.
[51] J.M. Lin, 'Python Non-Uniform Fast Fourier Transform (PyNUFFT): An Accelerated Non-Cartesian MRI Package on a Heterogeneous Platform (CPU/GPU)', *J. Imaging* 2018, 4(3): 51.
[52] S. Foucart and H. Rauhut, 'Algorithms for ℓ1-Minimization', in *A Mathematical Introduction to Compressive Sensing*, S. Foucart and H. Rauhut, Eds. New York, NY: Springer, 2013, pp. 475–513.
[53] W. van Aarle *et al.*, 'Fast and flexible X-ray tomography using the ASTRA toolbox', *Opt. Express* 2016, 24(22): 25129–25147.
[54] J. Nascimiento and J. M. Bioucas-Dias, 'Vertex component analysis: a fast algorithm, to unmix hyperspectral data', *IEEE Trans. Geosci. Remote Sens.* 2005, 43(4): 898–910.

[55] T. Sanders and R. B. Platte, 'Multiscale higher-order TV operators for L1 regularization', *Adv. Struct. Chem. Imaging* 2018, 4: 12.
[56] J.L. Starck, E. J. Candes and D. L. Donoho, 'The curvelet transform for image denoising', *IEEE Trans. Image Process.* 2002, 11(6): 670–684.
[57] T. Gebäck and P. Koumoutsakos, 'Edge detection in microscopy images using curvelets', *BMC Bioinformatics* 2009, 10(1): 75.
[58] J.L. Starck, D. Donoho and E.J. Candes, 'Very high quality image restoration by combining wavelets and curvelets', *Proc. SPIE - Int. Soc. Opt. Eng.* 2001, 4478.
[59] Z. Qu, X. Yan, J. Pan, and P. Chen, 'Sparse View CT Image Reconstruction Based on Total Variation and Wavelet Frame Regularization', *IEEE Access* 2020, 8: 57400–57413.
[60] Z. Saghi *et al.*, 'Compressed Sensing Electron Tomography of Needle-Shaped Biological Specimens-Potential for Improved Reconstruction Fidelity with Reduced Dose', *Ultramicroscopy* 2016, 160: 230-238.
[61] G. Ding, Y. Liu, R. Zhang, and H. L. Xin, 'A joint deep learning model to recover information and reduce artifacts in missing-wedge sinograms for electron tomography and beyond', *Sci. Rep.* 2019, 9: 12803.
[62] R. Tovey *et al.*, 'Directional Sinogram Inpainting for Limited Angle Tomography', *Inverse Probl.* 2019, 35: 024004.
[63] D.S. Weller, S. Ramani, J.F. Nielsen and J.A. Fessler, 'Monte Carlo SURE-based parameter selection for parallel magnetic resonance imaging reconstruction', *Magn. Reason. Med.* 2014, 71(5): 1760-1770.

Supplementary information

SI_movie_1: aligned GST (left) and Ge (right) stacks.

SI_movie_2: 2D slices through the TV (top) and Bior4.4 (bottom) reconstructions of the GST (left) and Ge (right) volumes.

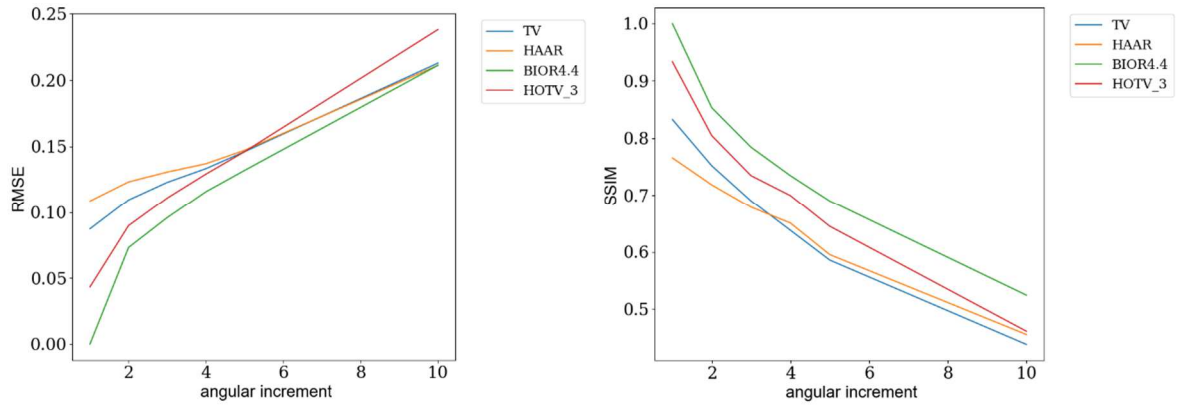

Figure S1 Performance of TV, Haar, HOTV and Bior4.4 approaches, using the Bior4.4 1° reconstruction as a reference image for all methods. RMSE (left) and SSIM (right) scores showing the evolution of the image quality as a function of the angular increment (in degrees).

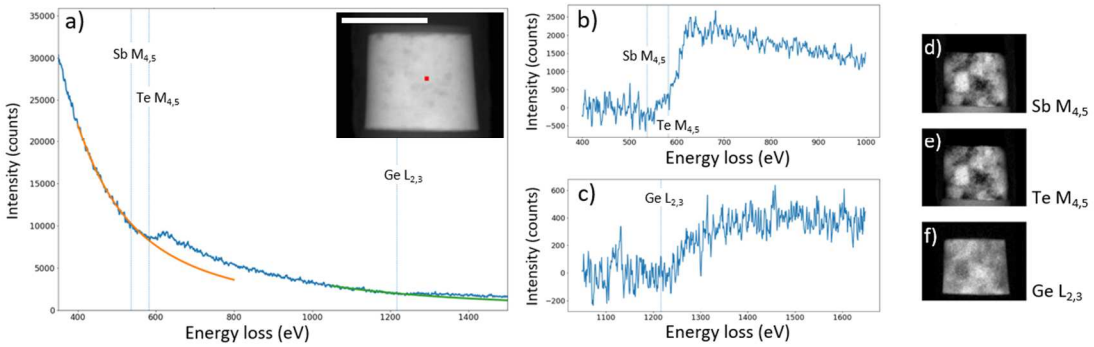

Figure S2 (a) Experimental EELS spectrum corresponding to the pixel indicated in red in the inset. Hyperspy was used to estimate the background (in orange for Sb $M_{4,5}$ and Te $M_{4,5}$, in green for Ge $L_{2,3}$). (b,c) Extracted signals after background subtraction. (d,e,f) Sb, Te and Ge elemental maps.

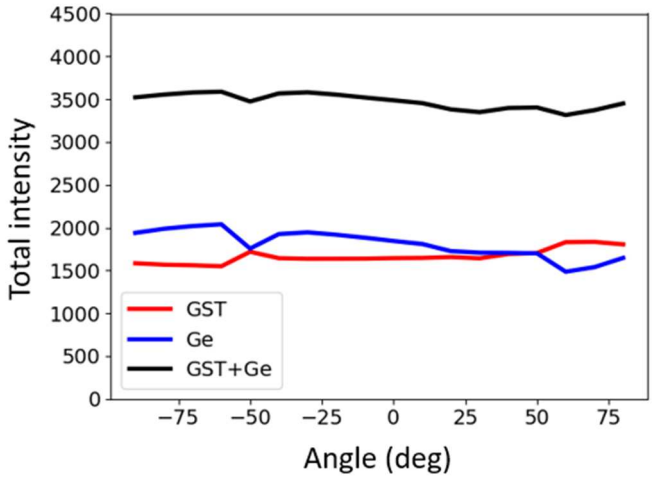

Figure S3 Total intensity of the projections corresponding to Ge (blue) and GST (blue) chemical phases, as function of the tilt angle. The sum of the two signals is shown in black.